

Thermal flux in unsteady Rayleigh-Bénard magnetoconvection

Sandip Das^a, Krishna Kumar^{a,*}

^a Department of Physics, Indian Institute of Technology Kharagpur, Kharagpur-721302, India

Abstract

We present results of numerical investigation on thermal flux in Rayleigh-Bénard magnetoconvection in the presence of a uniform vertical magnetic field. We have studied thermal flux in different viscous fluids with a range of Prandtl number ($0.1 \leq \text{Pr} < 6.5$) and a range of Chandrasekhar number ($50 \leq Q \leq 2.5 \times 10^4$). The power spectral density of the Nusselt number varies with frequency f approximately as f^{-2} . The probability distribution function of the fluctuating part of the Nusselt number is nearly normal distribution with slight asymmetric tails. For a fixed value the Rayleigh number Ra , the time averaged Nusselt number $\langle \text{Nu}(Q) \rangle$ decreases logarithmically with Chandrasekhar number for $Q > Q_c$, which depends on Ra and Pr . The reduced Nusselt number $\text{Nu}_r = \langle \text{Nu}(Q) \rangle / \langle \text{Nu}(0) \rangle$ rises sharply, reaches a maximum slightly above unity and then start decreasing very slowly to unity as the value of a dimensionless parameter $\sqrt{Ra/(Q\text{Pr})}$ is raised. The probability distribution function of the local thermal flux in the vertical direction is found to be asymmetric and non-Gaussian with a cusp at its maximum.

Keywords: Magnetoconvection, Rayleigh number, Chandrasekhar number, Nusselt number, local heat flux, thermal boundary layer, Power spectral density, nanofluids

1. Introduction

The understanding of heat flux in magnetoconvective flows is a topic of intense research due to its potential industrial applications in nanofluids [1–3], biofluids [4], electro-chemical process [5] and material processing research [5–7] in addition to its relevance in traditional areas like geophysics [8–12] and astrophysics [13–16]. A thermally stratified system, where a thin horizontal layer of a fluid is subjected to an adverse temperature gradient and simultaneously subjected to a uniform magnetic field, is known as Rayleigh-Bénard magnetoconvection (RBM) [17–20]. Chandrasekhar [17] analysed the linear problem of thermal convection in a homogeneous fluid. He showed that a uniform vertical magnetic field delays the convective flow. In addition, he showed that the onset of convection is always stationary if Pr is greater than Pm .

The dynamics of RBM is governed by four dimensionless quantities:

- (1) Rayleigh number Ra , which is the relative measure of the buoyancy force over the dissipative force,
- (2) Chandrasekhar's number Q , which is a measure of the strength of the Lorentz force,
- (3) the thermal Prandtl number $\text{Pr} = \nu/\kappa$ is a ratio of the effective kinematic viscosity ν and the effective thermal diffusivity κ , and
- (4) the effective magnetic Prandtl number $\text{Pm} = \sigma\mu_0\nu$, where σ is the electrical conductivity of the fluid and μ_0 is the magnetic permeability of air. The magnetic diffusivity of the fluid is defined as $\eta = 1/(\mu_0\sigma)$.

Experiments on the measurement of thermal flux in magnetoconvection in metallic fluids [21–23] showed that the transport of heat across the fluid layer in turbulent magnetoconvection was reduced significantly and the fluid flow was affected [20]. It was also found that the time averaged Nusselt number $\langle \text{Nu} \rangle$ showed scaling behaviour with Rayleigh number Ra [21, 22]. The scaling exponent was found to depend on the strength of the applied magnetic field. A uniform nanofluid consists of homogeneous suspension of metallic nanoparticles in an ordinary fluid, which is also known as a base/carrier fluid. The viscous, thermal, electrical and magnetic properties of a nanofluid depend on the properties of the base fluid as well as the properties of suspended nanoparticles. There is hardly any work on the role of magnetic field on the heat flux in unsteady flows in fluids including nanofluids, liquid crystals and metallic fluids.

In this article we present results of numerical simulations on both global and local heat fluxes in RBM with a uniform vertical magnetic field in water based nanofluids with low dilution of non-magnetic spherical nanoparticles. We have computed Nusselt number $\text{Nu}(Q)$, which is a measure of the global heat flux for non-zero value of Chandrasekhar's number Q , which is a ratio of the Lorentz force per unit volume to the drag force due to magneto-viscous effect. The time averaged Nusselt number $\langle \text{Nu}(Q) \rangle$ increases slowly with Chandrasekhar number Q for smaller values of Q . The effective Prandtl number of fluid is varied from $0.1 \leq \text{Pr} \leq 6.4$. As soon as Q is raised above a critical value Q_c , which depends on Ra and Pr , $\langle \text{Nu}(Q) \rangle$ decreases logarithmically with Q for a fixed value of Ra . We have also plotted the variation of the reduced Nusselt number $\text{Nu}_r = \langle \text{Nu}(Q) \rangle / \langle \text{Nu}(0) \rangle$ with a dimensionless parameter $\sqrt{Ra/(Q\text{Pr})}$, which is a ratio of the buoyancy and Lorentz forces. For fluids with Prandtl number $\text{Pr} \leq 4.0$, Nu_r increases sharply with

*Corresponding author

Email address: kumar.phy.iitkgp@gmail.com (Krishna Kumar)

the dimensionless parameter $\sqrt{\text{Ra}/(\text{QPr})}$. It attains a maximum slightly above unity and then begins decreasing slowly towards unity, as $\sqrt{\text{Ra}/(\text{QPr})}$ is further raised. The probability distribution of fluctuations in the Nusselt number is close to normal with slightly asymmetric tails. The probability distribution functions (PDF) of the local heat fluxes in the vertical direction are found to be non-Gaussian with a cusp at their maxima. PDFs are asymmetric about their maxima and have exponential tails.

2. Hydromagnetic System

We consider a thin horizontal layer of a homogeneous nanofluid of effective density ρ and thickness d , effective thermal expansion coefficient α and effective electrical conductivity σ and subjected to an adverse temperature gradient β in the presence of a uniform magnetic field $\mathbf{B}_0 = B_0 \mathbf{e}_3$ directed along the vertical direction. Here \mathbf{e}_3 is a unit vector in the vertically upward direction. The effective density ρ and the electrical conductivity σ are expressed [3] as:

$$\rho = (1 - \phi)\rho_f + \phi\rho_p, \quad (1)$$

$$\sigma = (1 - \phi)\sigma_f + \phi\sigma_p, \quad (2)$$

where ϕ is the volume fraction of the suspended spherically shaped nanoparticles of density ρ_p and electrical conductivity σ_p in a base fluid of density ρ_f and electrical conductivity σ_f . We may express the products $\rho\alpha$ and ρc_V for nanofluids [3] as:

$$(\rho\alpha) = (1 - \phi)(\rho\alpha)_f + \phi(\rho\alpha)_p, \quad (3)$$

$$(\rho c_V) = (1 - \phi)(\rho c_V)_f + \phi(\rho c_V)_p, \quad (4)$$

where c_V stands for the effective specific heat of nanofluid at constant volume. The effective thermal conductivity K of a nanofluid [24] with spherical nanoparticles of thermal conductivity K_p in a base fluid of thermal conductivity K_f is expressed as

$$K = K_f \left[\frac{(K_p + 2K_f) - 2\phi(K_f - K_p)}{(K_p + 2K_f) + \phi(K_f - K_p)} \right]. \quad (5)$$

Following Brinkman [25], the effective dynamic viscosity μ of a nanofluid may be modelled as:

$$\mu = \mu_f(1 - \phi)^{-2.5}, \quad (6)$$

where μ_f is the dynamic viscosity of the base fluid. All diffusion coefficients may then be computed using these expressions. The effective kinematic viscosity ν or the effective momentum diffusion coefficient of the nanofluid may be computed as:

$$\nu = \frac{\mu}{\rho} = \frac{\mu_f(1 - \phi)^{-2.5}}{(1 - \phi)\rho_f + \phi\rho_p}. \quad (7)$$

Similarly the effective thermal diffusion coefficient $\kappa = K/(\rho c_V)$ of a nanofluid with spherical non-magnetic metallic particles may be computed using the expression:

$$\kappa = \frac{K_f}{[(1 - \phi)(\rho c_V)_f + \phi(\rho c_V)_p]} \times \left[\frac{(K_p + 2K_f) - 2\phi(K_f - K_p)}{(K_p + 2K_f) + \phi(K_f - K_p)} \right]. \quad (8)$$

Initially the fluid is at rest and the heat flux across the fluid layer is only due to conduction. The lower boundary of the nanofluid is maintained at temperature T_b , while the upper boundary is maintained at temperature $T_u = T_b - \Delta T$. Here, $\beta = (T_u - T_b)/d = \Delta T/d < 0$. The steady state temperature profile $T_s(z)$, density stratification $\rho_s(z)$ and the pressure field $P_s(z)$ across the nanofluid in conduction state [17] are given by,

$$T_s(z) = T_b + \beta z, \quad (9)$$

$$\rho_s(z) = \rho_0 [1 + \alpha (T_b - T_s(z))], \quad (10)$$

$$P_s(z) = P_0 - \rho_0 g \left(z + \frac{1}{2} \alpha \beta z^2 \right), \quad (11)$$

where T_b and ρ_0 are the reference values of the temperature and density fields at the bottom surface of the nanofluid. P_0 is a constant, which includes the magnetic pressure. As soon as β is raised above a critical value β_c , the basic state of conduction becomes unstable and convective flow ($\mathbf{v} \neq 0$) begins. All the fields are perturbed and may be written as:

$$\rho_s(z) \rightarrow \tilde{\rho}(x, y, z, t) = \rho_s(z) + \delta\rho(x, y, z, t), \quad (12)$$

$$T_s(z) \rightarrow T(x, y, z, t) = T_s(z) + \theta(x, y, z, t), \quad (13)$$

$$P_s(z) \rightarrow P(x, y, z, t) = P_s(z) + p(x, y, z, t), \quad (14)$$

$$\mathbf{B}_0 \rightarrow \mathbf{B}(x, y, z, t) = \mathbf{B}_0 + \mathbf{b}(x, y, z, t). \quad (15)$$

All length scales are measured in units of the fluid thickness d and time is measured in units of the free-fall time $\tau_f = 1/\sqrt{\alpha g \beta}$, where g is the acceleration due to gravity. The fluid velocity $\mathbf{v}(x, y, z, t) = (v_1, v_2, v_3)^T$, the perturbation in pressure due to flow $p(x, y, z, t)$, the convective temperature $\theta(x, y, z, t)$ and the induced magnetic field $\mathbf{b}(x, y, z, t)$ are made dimensionless by $\sqrt{\alpha g \beta d^2}$, $\rho_0 \alpha g \beta d^2$, βd and $\nu \sigma \mu_0 B_0$, respectively. The value of the effective magnetic Prandtl number Pm is of the order of 10^{-5} or less for terrestrial fluids including nanofluids. We therefore set the value of Pm equal to zero in this work. This makes the induced magnetic field \mathbf{b} a slaved variable. The RBM in nanofluids is then described by the following dimensionless equations:

$$D_t \mathbf{v} = -\nabla p + \sqrt{\frac{\text{Pr}}{\text{Ra}}} \nabla^2 \mathbf{v} + \frac{\text{QPr}}{\text{Ra}} \partial_z \mathbf{b} + \theta \mathbf{e}_3, \quad (16)$$

$$\nabla^2 \mathbf{b} = -\sqrt{\frac{\text{Ra}}{\text{Pr}}} \partial_z \mathbf{v}, \quad (17)$$

$$D_t \theta = \sqrt{\frac{1}{\text{RaPr}}} \nabla^2 \theta + v_3, \quad (18)$$

$$\nabla \cdot \mathbf{v} = \nabla \cdot \mathbf{b} = 0, \quad (19)$$

where $D_t \equiv \partial_t + (\mathbf{v} \cdot \nabla)$ is the material derivative. In the above the dimensionless number Rayleigh number Ra is defined as $Ra = \frac{\alpha \beta g d^4}{\nu \kappa} = \frac{\rho_0 g \alpha \beta d}{(\rho_0 \nu \kappa / d^3)}$. It is a ratio of the buoyancy force per unit volume to the drag force per unit volume due to thermo-viscous effect. Other dimensionless external parameter for magnetoconvection is the Chandrasekhar's number Q , which is a measure of the strength of the external magnetic field and it is a ratio of the Lorentz force per unit volume to the drag force due to magneto-viscous effect. It is defined as $Q = \frac{\sigma B_0^2 d^2}{\rho_0 \nu} = \frac{B_0^2 / (\mu_0 d)}{(\rho_0 \nu \eta / d^3)}$. It is also equal to square of the Hartmann number $H = B_0 d \sqrt{\sigma / (\rho_0 \kappa)}$. It plays the role which Taylor number plays in RBC with Coriolis force [17].

Horizontal boundaries, located at $z = 0$ and $z = 1$, are considered to be thermally conducting and electrically nonconducting. Teflon or ethylene-vinyl-acetate (EVA) composites may realize these conditions in an experiment [26]. Horizontal boundaries made of good thermal conducting material and maintained at constant temperatures do not allow temperature fluctuations at the boundaries due to convective flow in the fluid. So the convective temperature field θ vanishes at the boundaries. Electrically nonconducting surfaces do not allow current across the surface. Therefore, the vertical component of the current density $\mathbf{j} = (\nabla \times \mathbf{b}) / \mu_0$ should also vanish at the horizontal boundaries. In addition, the induced magnetic field should be continuous at the boundaries. The induced magnetic field \mathbf{b}^p in an electrically non-conducting plate of permeability μ_p must be derivable from a potential [17]. That is,

$$\mathbf{b} = \mathbf{b}^p \text{ at } z = 0, 1, \text{ where} \quad (20)$$

$$\mathbf{b}^p = \nabla \Psi, \text{ where } \nabla^2 \Psi = 0. \quad (21)$$

In the limit $Pm \rightarrow 0$, as considered here, the boundary conditions of the induced magnetic field \mathbf{b} are dictated by Eq. 17. This equation is satisfied when b_1 , b_2 and $\partial_z b_3$ vanish at the horizontal boundaries. This choice also ensures that $j_3 = 0$ and $\nabla \cdot \mathbf{b} = 0$ are automatically satisfied. The velocity boundary conditions on horizontal boundaries are assumed to be *stress-free*, which are idealized boundary conditions. A good approximation for stress-free boundary conditions were realized in experiments by Goldstein and Graham [27]. RBM at higher values of Chandrasekhar's number Q flows are not affected significantly due to stress-free boundary conditions. The relevant boundary conditions [17] are then given as:

$$\partial_z v_1 = \partial_z v_2 = v_3 = b_1 = b_2 = \partial_z b_3 = \theta = 0 \text{ at } z = 0, 1. \quad (22)$$

Let us denote magnetic field in the upper boundary as $\mathbf{b}|_{z=1}$ and the same in the lower boundary as $\mathbf{b}|_{z=0}$, respectively. Then

$$\mathbf{b}|_{z=1} = \nabla \Psi|_{z=1} \text{ and } \mathbf{b}|_{z=0} = \nabla \Psi|_{z=0}, \quad (23)$$

where $\Psi|_{z=1}$ and $\Psi|_{z=0}$ are scalar potentials in the regions $z > 1$ and $z < 0$, respectively. The non-zero horizontal velocities of a nanofluid at the stress-free boundaries allow surface currents at the horizontal boundaries. The continuity of the vertical component of the induced magnetic field at the horizontal boundaries ($z = 0, 1$) fixes the horizontal current.

The effective thermal Prandtl number of the water based nanofluids may be varied from 6.5 to 4.0, if the volume fraction

of spherical copper nanoparticles are varied from 0.2% to 8.0%. The set of hydromagnetic system (Eqs. 16-22) is applicable to water based homogeneous nanofluids with non-magnetic metallic particles. In the absence of nanoparticles ($\phi = 0$), the hydrodynamic system represents magnetoconvection in geophysical fluids. The value of Pr for Earth's liquid outer core is approximated to be in a range from 0.1 to 10 [8]. Some liquid crystals have $Pr \sim 4.0$. These equations may also be useful in electrically conducting gases. The gases at high temperatures may conduct electricity as in a discharge tube. The range of Pr is chosen to cover different types of fluids. The critical Rayleigh number $Ra_c(Q)$ for the onset of stationary magnetoconvection depends on the Chandrasekhar's number Q . The critical wave number $k_c(Q)$, which is the wave number at the onset of convection, also depends on Q . The expressions for $Ra_c(Q)$ and $k_c(Q)$ are:

$$Ra_c(Q) = \frac{\pi^2 + k_c^2}{k_c^2} [(\pi^2 + k_c^2)^2 + \pi^2 Q], \quad (24)$$

$$k_c(Q) = \pi \sqrt{a_+ + a_- - \frac{1}{2}}, \quad (25)$$

$$a_{\pm} = \left(\frac{1}{4} \left[\frac{1}{2} + \frac{Q}{\pi^2} \pm \left[\left(\frac{1}{2} + \frac{Q}{\pi^2} \right)^2 - \frac{1}{4} \right]^{\frac{1}{2}} \right] \right)^{\frac{1}{3}}, \quad (26)$$

The global heat flux across the fluid layer is defined by Nusselt number Nu , which is a ratio of spatially averaged the total heat flux and the conductive heat flux. It is defined in terms of dimensionless vertical velocity v_3 and convective temperature θ as:

$$Nu(t) = 1 + \frac{\sqrt{Ra} Pr}{V} \int_0^{\frac{2\pi}{k_c}} \int_0^{\frac{2\pi}{k_c}} \int_0^1 v_3 \theta dx dy dz, \quad (27)$$

where $V = 4\pi^2 / k_c^2$ is the dimensionless volume of the simulation box. The Nusselt number, which is a function of time for unsteady magnetoconvection, depends on Ra , Pr and Q . Its time averaged value over a long period T is denoted as $\langle Nu \rangle = \frac{1}{T} \int_0^T Nu(t) dt$. The quantity $v_3 \theta$ represents the local heat flux in the vertical direction due to magnetoconvection.

3. Direct Numerical Simulations

Direct numerical simulations are done using pseudo-spectral method. All fields are assumed to be periodic in the horizontal plane. The expansion of the relevant perturbations, consistent with the boundary conditions considered, are:

$$v_1(x, y, z, t) = \sum_{l, m, n} U_{lmn}(t) e^{ik(lx+my)} \cos(n\pi z), \quad (28)$$

$$v_2(x, y, z, t) = \sum_{l, m, n} V_{lmn}(t) e^{ik(lx+my)} \cos(n\pi z), \quad (29)$$

$$v_3(x, y, z, t) = \sum_{l, m, n} W_{lmn}(t) e^{ik(lx+my)} \sin(n\pi z), \quad (30)$$

$$\theta(x, y, z, t) = \sum_{l, m, n} \Theta_{lmn}(t) e^{ik(lx+my)} \sin(n\pi z), \quad (31)$$

$$p(x, y, z, t) = \sum_{l, m, n} P_{lmn}(t) e^{ik(lx+my)} \cos(n\pi z), \quad (32)$$

Pr	Ra	Q	Nu	ϵ'' (est.)	ϵ'' (comp.)	ϵ^θ (est.)	ϵ^θ (comp.)	Nu _{kin}	Nu _{th}
1.0	3.04×10^6	0	19.76	0.0107	0.0107	0.0113	0.0112	19.66	19.56
		300	20.44	0.0111	0.0110	0.0117	0.0115	20.18	20.10
		700	20.59	0.0112	0.0111	0.0118	0.0116	20.35	20.23
4.0	5.0×10^5	0	13.53	0.0088	0.0088	0.0095	0.0095	13.45	13.40
		100	13.63	0.0089	0.0089	0.0096	0.0094	13.58	13.30
		300	11.80	0.0076	0.0075	0.0083	0.0081	11.61	11.46
		500	10.85	0.0069	0.0068	0.0076	0.0074	10.62	10.46
6.4	5.0×10^5	0	14.31	0.0074	0.0074	0.0079	0.0079	14.24	14.17
		100	13.41	0.0069	0.0068	0.0074	0.0073	13.16	13.06
		300	11.43	0.0058	0.0057	0.0063	0.0062	11.20	11.09
		500	10.78	0.0054	0.0053	0.0060	0.0058	10.48	10.37

Table 1: List of Nusselt number Nu(Q) for different values of Chandrasekhar's number Q, kinetic energy dissipation rate ϵ'' and 'thermal energy' dissipation rate ϵ^θ . These dissipation rates are compared with their estimated values using the formulas $\epsilon'' = (\text{Nu} - 1)/\sqrt{\text{RaPr}}$ and $\epsilon^\theta = \text{Nu}/\sqrt{\text{RaPr}}$.

where $U_{lmn}(t)$, $V_{lmn}(t)$, $W_{lmn}(t)$, $\Theta_{lmn}(t)$, and $P_{lmn}(t)$ are the Fourier amplitudes in the expansion of the fields v_1 , v_2 , v_3 , θ , and p respectively. The wave vector of perturbations in the horizontal plane is $\mathbf{k} = l\mathbf{e}_1 + m\mathbf{e}_2$. We have set $k = k_c(Q)$, where $k_c(Q)$ is the critical wave number for a given value of Q. The integers l, m, n can take values compatible with continuity equation, which leads to the following condition.

$$ilk_c(Q)U_{lmn} + imk_c(Q)V_{lmn} + n\pi W_{lmn} = 0. \quad (33)$$

The expansions of the magnetic fields in the boundaries outside the nanofluids [20] may be expressed as:

$$\Psi|_{z \geq 1} = \sum_{l,m,n} (-1)^{n+1} \Psi_{lmn}(t) e^{ik(lx+my)} e^{\gamma(1-z)}, \quad (34)$$

$$\Psi|_{z \leq 0} = \sum_{l,m,n} \Psi_{lmn}(t) e^{ik(lx+my)} e^{\gamma z}, \quad (35)$$

where $\gamma = k\sqrt{l^2 + m^2}$ and $\Psi_{lmn}(t) = \frac{n\pi W_{lmn}(t)}{\gamma(\gamma^2 + n^2\pi^2)}$. The spatial grid resolutions of the periodic box of size $L \times L \times 1$, where $L = 2\pi/k_c(Q)$. Spatial resolution of $128 \times 128 \times 128$ or $256 \times 256 \times 256$ grid points has been used for simulations presented here. As the Rayleigh number is raised above a critical value $\text{Ra}_c(Q)$, while keeping the values of Q and Pr fixed, stationary magnetoconvection begins [17]. We define the distance from criticality by a parameter $\epsilon = \frac{\text{Ra} - \text{Ra}_c(Q)}{\text{Ra}_c(Q)}$. As Q is raised keeping Ra and Pr fixed, the parameter ϵ becomes smaller and consequently the fluctuations are reduced. The fluctuations are

more at lower values of Q, if the value of Ra is sufficiently raised. As a results the spatial resolution required is less, if Q is raised to a higher value with Ra and Pr fixed. The spatial resolutions used here are sufficient to describe the magnetoconvective flow for the parameter values considered. We have compared our results for Q = 0 with those obtained by Veronis [28], Moore & Weiss [29] and Thual [30], who used the identical boundary conditions. The two sets of grid resolutions used here keep the minimum value of the global Kolmogorov dissipative scale always more than 2. We have also reproduced the results reported in the earlier works on magnetoconvective instability [20] as well as on RBC [31]. Of course, for much lower values of Pr (< 0.1) and much higher values of Ra would require better spatial grid resolutions. We have listed in Table 1 values of Nusselt number Nu(Q), the average dissipative rates for the kinetic energy $\epsilon'' = \langle \nu \int_0^{2\pi} \int_0^{2\pi} \int_0^1 \{\partial_i v_j(x, y, z, t)\}^2 dx dy dz \rangle$ and 'thermal energy' $\epsilon^\theta = \langle \kappa \int_0^{2\pi} \int_0^{2\pi} \int_0^1 \{\partial_i \theta(x, y, z, t)\}^2 dx dy dz \rangle$ for different values of Chandrasekhar's number Q. The computed values of the dissipation rates ϵ'' and ϵ^θ are compared with their estimated values using the formulas: $\epsilon'' = (\text{Nu}(Q) - 1)/\sqrt{\text{RaPr}}$ and $\epsilon^\theta = \text{Nu}(Q)/\sqrt{\text{RaPr}}$ in Table 1. They are in good agreement. Rayleigh-Bénard convection was investigated numerically in a cubic box with no-slip velocity boundary conditions on all walls by Xu et al [32]. Their velocity boundary conditions and simulation box size were different than what we have

considered here. The values for the Nusselt number in a fluid with $Pr = 7.0$ are 8.49 and 11.12 for $Ra = 10^6$ and 3×10^6 , respectively. Our values for Nusselt number are almost double (17.32 for $Ra = 10^6$ and 23.54 for $Ra = 3 \times 10^6$). The definitions of the dissipation rate for kinetic energy also differs by a numerical factor of $1/2$.

We record the values of all relevant fields at all spatial grid points at a regular interval of every two units of dimensionless time. We have computed minimum number of 300 frames for each set of parameter values reported here.

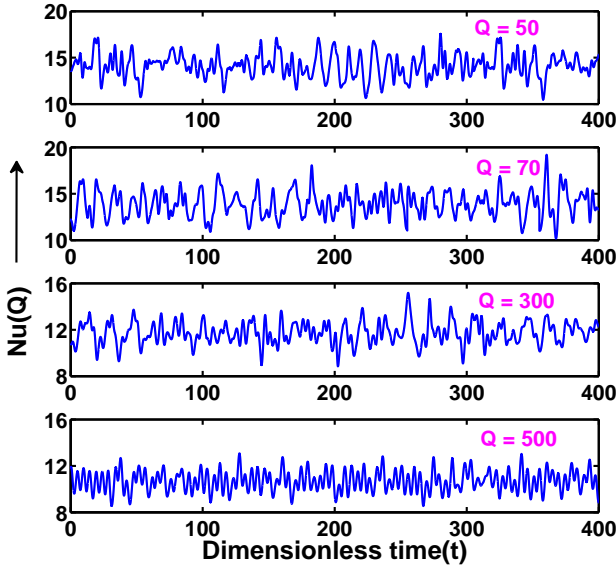


Figure 1: (Color online) Variation of Nusselt number $Nu(Q)$ with dimensionless time t [blue (black) curves] for Rayleigh number $Ra = 5.0 \times 10^5$ and Prandtl number $Pr = 4.0$ for different values of Chandrasekhar number Q .

4. Results and Discussions

As Rayleigh number Ra is raised to a sufficiently high value for fixed values of Chandrasekhar number Q and Prandtl number Pr , the magnetoconvection becomes unsteady. Fig 1 shows the variation of Nusselt number for chaotic magnetoconvective flow with dimensionless time for $Ra = 5.0 \times 10^5$ and $Pr = 4.0$ for different values of Q . The temporal evolution of Nusselt number for $Q = 70, 300, 500$ show that the time averaged mean value $Nu(Q)$ decreases with increase in Q . It confirms that the magnetic field suppresses the heat flux of in RBM at relatively larger values of Q . Figure 2 shows typical three-dimensional isosurfaces computed at a given instant from the DNS for $Ra = 5 \times 10^5$ and $Pr = 4.0$ for two different values of Q . More thermal plumes are generated for $Q = 70$ than for $Q = 500$. The generation of more thermal plumes leads to enhancement of the relative Nusselt number in a range of lower values of Q for fixed values of Ra and Pr .

The temporal fluctuation of Nusselt number is considerable for lower values of Q (see Fig. 1). Figure 3 displays the standard

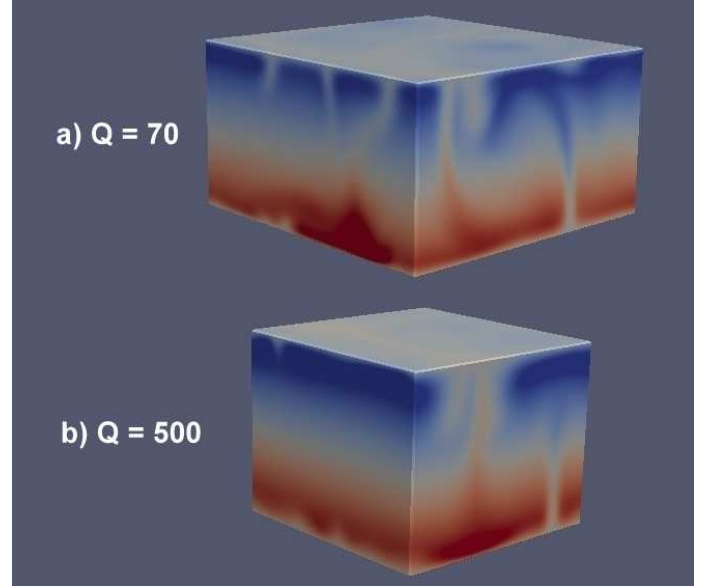


Figure 2: (Color online) Three-dimensional temperature isosurfaces computed from DNS for $Ra = 5.0 \times 10^5$ and $Pr = 4.0$ for (a) $Q = 70$ and (b) $Q = 500$. Red (grey) and blue (black) colors stand for hotter and cooler fluids, respectively.

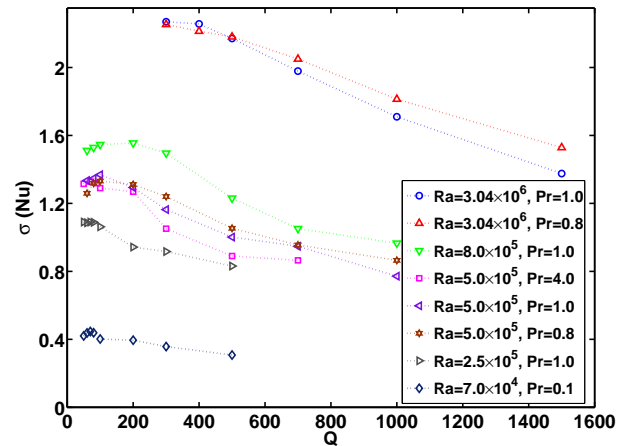


Figure 3: (Color online) Standard deviation $\sigma(Nu)$ of the Nusselt number Nu for different values of Ra , Pr and Q .

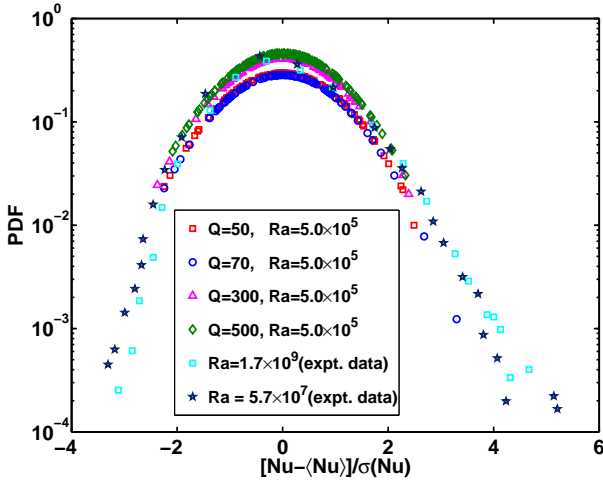


Figure 4: (Color online) Probability density function (PDF) of the fluctuations in Nusselt number Nu at $Ra = 5.0 \times 10^5$ and $Pr = 4.0$ for different values of Q . Red (gray) squares, blue (black) circles, magenta (dark gray) triangles and green (gray) diamonds are for $Q = 50, 70, 300$ and 500 , respectively. Blue (black) stars and cyan (light gray) squares are experimental data points (Ref. [33]) in absence of the external magnetic field ($Q = 0$) for $Ra = 5.7 \times 10^7$ and 1.7×10^9 , respectively.

deviation in the temporal signals of Nusselt number for different values of Ra , Pr and Q . Fluctuations are larger at higher values Ra . Fluids with lower values of effective thermal Prandtl number Pr show relatively larger fluctuations. The fluctuations are suppressed at higher values of the applied magnetic field, if all other parameters are kept fixed. For higher values of Q , the distance from the onset of magnetoconvection is smaller and, consequently, the fluctuating part of the Nusselt number is reduced.

Figure 4 shows the probability distribution function (PDF) of the fluctuating parts of the Nusselt number around the mean for different values of Q . Probability distribution function is close to normal distribution but with slightly asymmetric tails. For effective value of $Pr = 4$, the height of PDF is the lowest for $Q = 70$ but tails are longer. As Q is increased or decreased, the height of PDF goes up and tails become shorter. We have also compared the computed PDFs with the experimental results of Aumaitre and Fauve [33] on Rayleigh-Bénard convection (RBC) in water and mercury in the absence of external magnetic field. The data points shown by navy blue (black) stars and cyan (light gray) squares are adopted from their experiments at much higher values of Ra . PDFs obtained for RBM are in good agreement with those observed in RBC in water and mercury. The slight difference is due to small Rayleigh number used for simulations. The computed curves are smoother due to large number of data points.

Figure 5 shows the power spectrum density (PSD) in the frequency space of the Nusselt number for $Ra = 5.0 \times 10^5$ and $Pr = 4.0$ and for different values of Q . The PSD shows noisy behaviour at lower frequencies. However, the Nusselt number is found to show scaling behaviour at higher frequencies. The

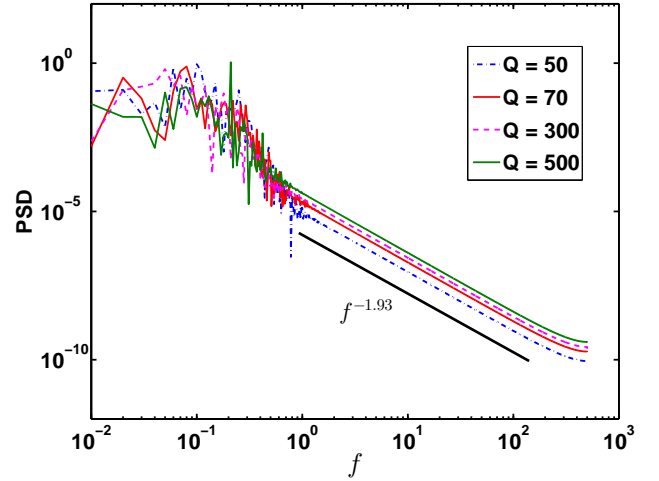


Figure 5: (Color online) Frequency power spectral density (PSD) of the Nusselt number (Nu) for $Ra = 5.0 \times 10^5$ and $Pr = 4.0$ at different values of Q .

PSD of Nu scales with frequency f approximately as f^{-2} . The best fit to curves obtained from simulations gives the value of the exponent as -1.93 ± 0.02 . The value of the exponent is quite close to one observed in experiments on turbulent RBC [33] as well as in numerical simulations of turbulent RBC with rotation [34].

The upper viewgraph in Fig. 6 displays the variation of time averaged Nusselt number $\langle Nu(Q) \rangle$ with Chandrasekhar number Q for several values of Ra and Pr on a semi-log scale. The magenta (very light gray), green (light gray), blue (black), brown (dark gray) and violet (gray) curves are the best fit to the data points obtained from simulations for different curves. Cyan (light gray) diamonds, blue (black) circles and red (gray) triangles at the top are the data points computed for $Pr = 2.0, 1.0$ and 0.8 , respectively. The green (gray) inverted triangles represent the data points computed for $Pr = 1.0$ in the second data set from top ($Ra = 8.0 \times 10^5$). Brown (dark gray) stars, violet (gray) left pointing triangles, magenta (light gray) squares and green (gray) stars in the third data set ($Ra = 5.0 \times 10^5$) are computed for $Pr = 0.8, 1.0, 4.0$ and 6.4 , respectively. Data points, shown as azure (gray) right pointing triangles in the fourth data set from the top ($Ra = 2.5 \times 10^5$), are for $Pr = 1.0$. Data points, shown as blue (black) diamonds and black (black) squares in the data set at the bottom are for $Pr = 0.1$ and $Pr = 0.2$, respectively. The lower viewgraph in Figure 6 shows the plot of threshold $Ra_c(Q)$ for stationary magnetoconvection with Q , as obtained by Chandrasekhar [17] for stress-free velocity boundary conditions. The time averaged value of the Nusselt number $\langle Nu(Q) \rangle$, for fixed values of Ra and Pr , first increases very slowly with Q , reaches a maximum and then starts decreasing quickly with Q . The tendency of slight enhancement of heat flux was not observed for $Pr = 6.4$. It has some similarity with enhancement of thermal flux at low rotation rates in rotating RBC. Fig. 6 also shows that decrease of $\langle Nu(Q) \rangle$ with Q is logarithmic for higher values of Q [see the magenta

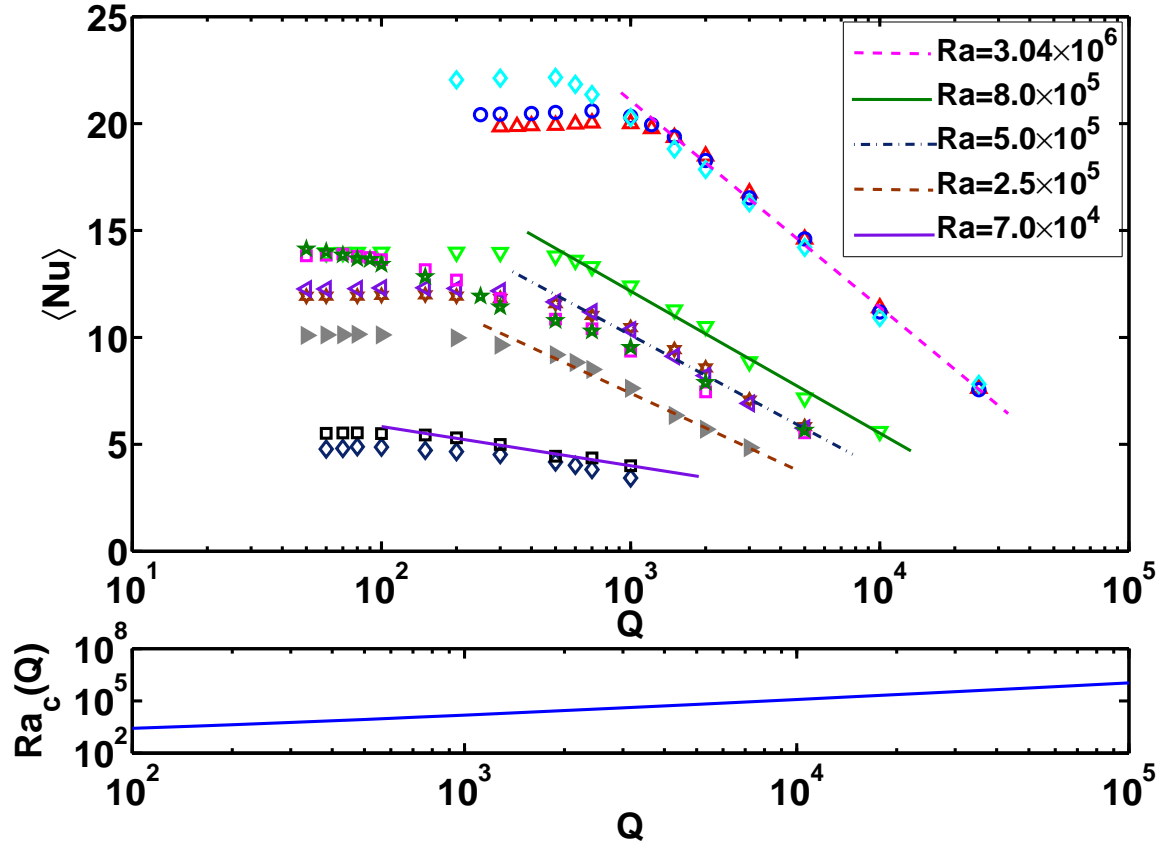


Figure 6: (Color online) The variation of time averaged Nusselt number $\langle Nu \rangle$ with Chandrasekhar's number Q for different values of Ra and Pr is shown in the upper viewgraph. The data set at the top is for $Ra = 3.04 \times 10^6$. Data points shown by cyan (light gray) diamonds, blue (black) circles and red (dark gray) triangles are computed for $Pr = 2.0, 1.0$ and 0.8 , respectively. The second set of computed data points from the top [green (gray) inverted triangles] are for $Ra = 8.0 \times 10^5$ and $Pr = 1.0$. The third data set from the top is for $Ra = 5.0 \times 10^5$. Here, brown (dark gray) stars, violet (gray) left pointing triangles, magenta (light gray) squares and green (gray) stars are data points computed for $Pr = 0.8, 1.0, 4.0$ and 6.4 respectively. The fourth data set from the top [azure (gray) right pointing triangles] is for $Ra = 2.5 \times 10^5$ and $Pr = 1.0$. The set of data points at the bottom are for $Ra = 7.0 \times 10^4$. Here blue (black) diamonds and black (black) squares are data points computed for $Pr = 0.1$ and $Pr = 0.2$, respectively. The lower viewgraph shows the plot of the threshold $Ra_c(Q)$ with Q .

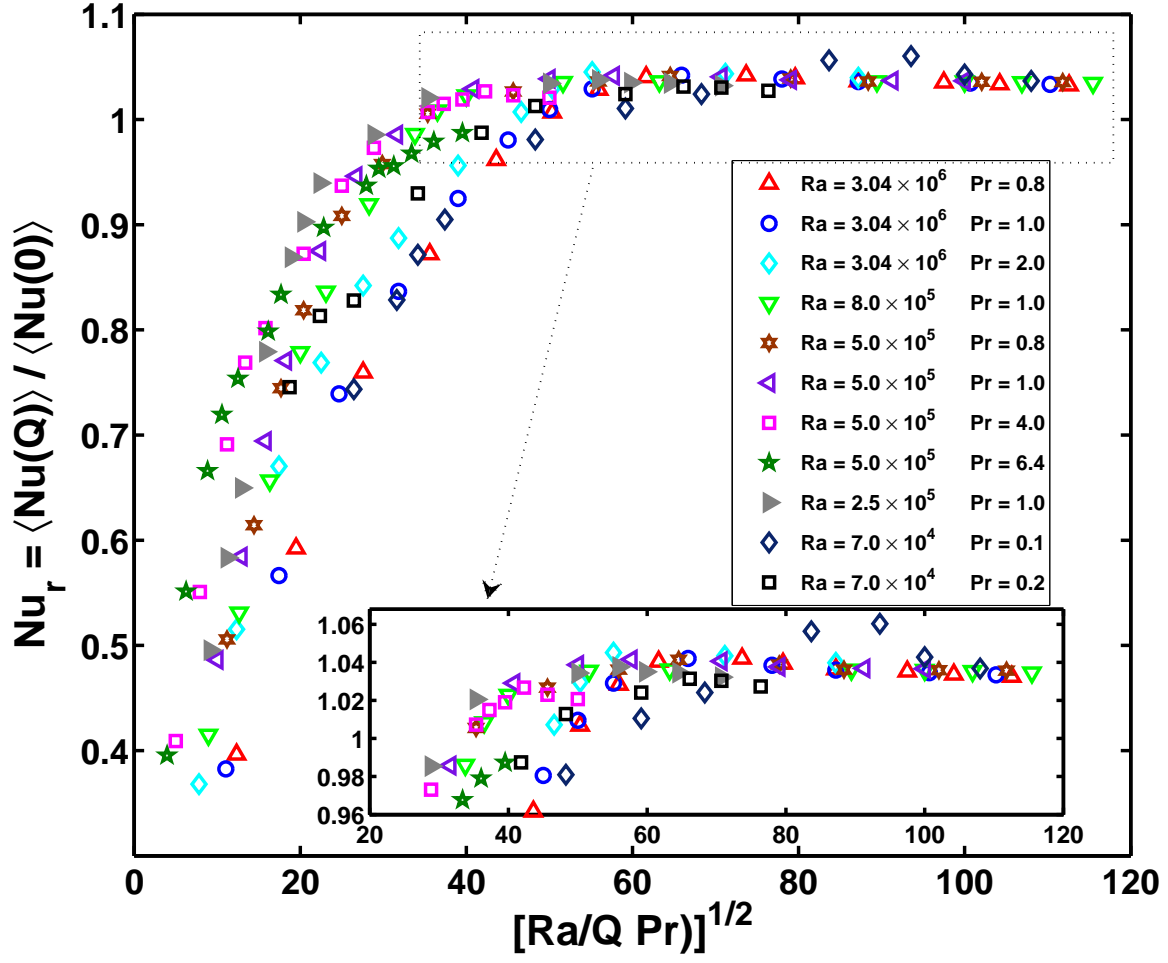


Figure 7: (Color online) Variation of the reduced Nusselt number $Nu_r = \langle Nu(Q) \rangle / \langle Nu(0) \rangle$ with the dimensionless quantity $\sqrt{Ra/(QPr)}$ for several sets of Ra and Pr : (i) $Pr = 0.1$ with $Ra = 7.0 \times 10^4$ [blue (black) diamonds], (ii) $Pr = 0.2$ with $Ra = 7.0 \times 10^4$ [black (black) squares], (iii) $Pr = 0.8$ and $Ra = 3.04 \times 10^6$ [red (gray) triangles] and 5.0×10^5 [brown (dark gray) stars], (iv) $Pr = 1.0$ with $Ra = 3.04 \times 10^6$ [blue (black) circles], 8.0×10^5 [green (light gray) inverted triangles], 5.0×10^5 [violet (gray) left pointing triangles] and 2.5×10^5 [azure (gray) right pointing triangles], (v) $Pr = 2.0$ with $Ra = 3.04 \times 10^6$ [cyan (light gray) diamonds], (vi) $Pr = 4.0$ with $Ra = 5.0 \times 10^5$ [magenta (light gray) squares] and (vii) $Pr = 6.4$ with $Ra = 5.0 \times 10^5$ [green (gray) stars]. Inset shows the enlarged view of the plot for $Nu_r \approx 1.0$.

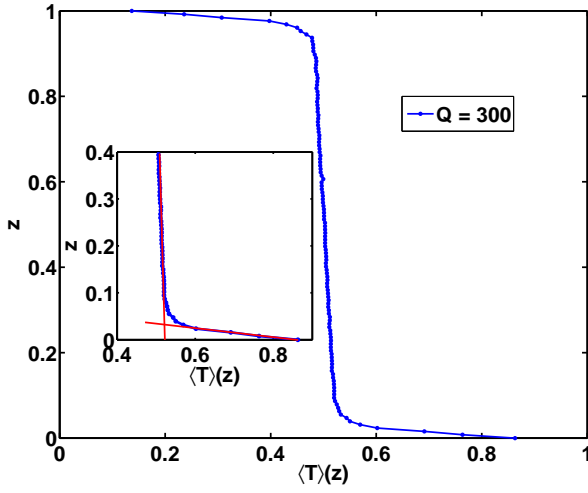


Figure 8: (Color online) Variations of horizontally averaged temperature field $\langle T \rangle(z)$ fields with the vertical coordinate are plotted for $Q = 300$ [blue (black) circle], for $Pr = 1.0$ and $Ra = 3.04 \times 10^6$. Red (gray) straight lines show the variations of temperature in the central part and near the lower boundary.

(light gray), green (gray), blue (black) and brown (dark gray) lines]. For given values of Q and Pr , the mean Nusselt number is higher for larger values of Ra . The effect of Pr is clearly visible only for $Q < Q_c$ (where $Q = Q_c$ denotes the critical value of Chandrasekhar number, above which the logarithmic behaviour starts to set in), if Ra is kept fixed. For $Q < Q_c$, $\langle Nu \rangle$ increases with Pr . There is no significant change in $\langle Nu \rangle$ for $Q > Q_c$ with Pr , if Ra is kept fixed. However, Nu_c (the critical value of time averaged Nusselt number at Q_c) increases but Q_c decreases with Pr for a fixed value of Ra . The values of Nu_c and Q_c both increases with Ra . For $Pr = 1.0$, we observe that Nu_c and Q_c vary with Ra as $Ra^{0.28 \pm 0.01}$ and $Ra^{0.65 \pm 0.03}$, respectively. For $Q > Q_c$, the Lorentz force starts playing dominant role on the heatflux across the fluid layer. On the other hand, the role of Lorentz force is less significant for $Q < Q_c$.

The slope of the $\langle Nu(Q) \rangle - Q$ curves for Q depends mainly on Ra . The time averaged Nusselt number for $Q > Q_c$ may therefore be expressed as:

$$\langle Nu(Q) \rangle = C_1(Ra, Pr) - C_2(Ra, Pr) \ln Q, \quad (36)$$

where C_1 and C_2 are functions of Ra and Pr .

We now define a reduced (or normalized) Nusselt number $Nu_r = \langle Nu(Q) \rangle / \langle Nu(0) \rangle$ as a ratio of the Nusselt number in the presence of an external magnetic field ($Q \neq 0$) and the Nusselt number $Nu(0)$ in the absence of any external magnetic field ($Q = 0$). The dimensionless parameter $Ra/(QPr)$ is a ratio of the buoyancy force per unit volume ($\alpha \beta g d^4 \rho_0$) and the Lorentz force per unit volume ($\sigma B_0^2 d^2 \nu$). If the vertical magnetic field always suppressed the transport of heat across the fluid layer [17, 21–23], the value of Nu_r should always be less than unity and it should approach asymptotically to unity as the parameter $\sqrt{Ra/(QPr)}$ is raised to a much larger value. Fig. 7 shows the variation of Nu_r with $\sqrt{Ra/(QPr)}$ for different values

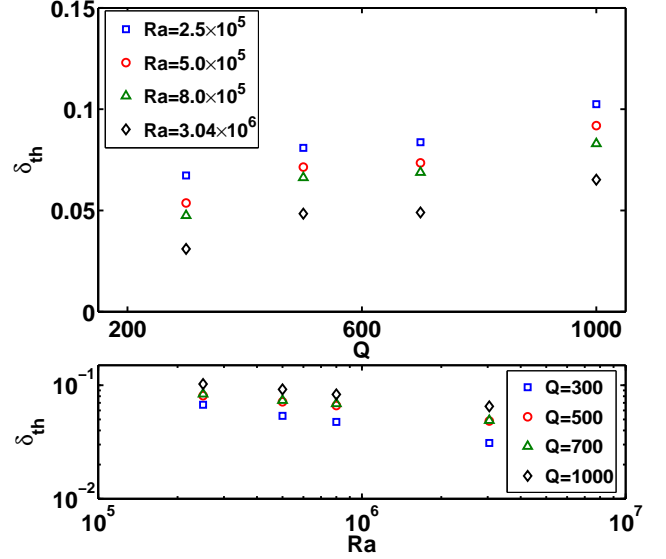


Figure 9: (Color online) Thermal boundary layer: Plot of the thickness of thermal boundary layer (δ_{th}) computed for $Pr = 1.0$ and Ra and Q . The upper viewgraph shows the variation of δ_{th} with Q for different values of Ra . The lower viewgraph shows variation of δ_{th} with Ra (on log-log scale) for different values of Q .

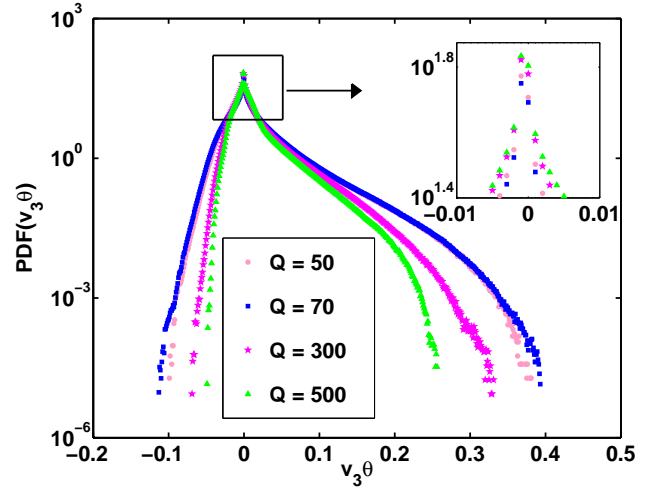


Figure 10: (Color online) The probability distribution functions (PDFs) of vertical heat flux for $Pr = 4.0$ computed for $Q = 50$ [pink (light gray) circles], 70 [blue (black) squares], 300 [magenta (gray) stars], and 500 [green (gray) triangles] with $Ra = 5.0 \times 10^5$. Inset shows the PDFs near their maxima.

of Pr . Nu_r increases sharply from a small value ($\ll 1$) and attains a value slightly bigger than unity, as $\sqrt{Ra/(QPr)}$ is raised slowly. With further increase in $\sqrt{Ra/(QPr)}$, the value of Nu_r starts decreasing slowly and tends to approach unity (see the plots for $Pr = 0.8, 1.0, 4.0$) slowly. The inset in Fig. 7 shows an enlarged view of the curve showing Nu_r more than unity. The maximum enhancement of thermal flux is observed for $0.1 \leq Pr \leq 4.0$. The value of the parameter $\sqrt{Ra/(QPr)}$, where Nu_r reaches its maximum, depends on Ra and Pr . We do not observe enhancement of thermal flux for $Pr = 6.4$. For lower

values of Q and for a range of Pr , the enhancement of thermal flux is observed in the unsteady magnetoconvection. This behaviour has similarity with enhancement of thermal flux observed in rotating RBC at lower values Rossby number (higher rotation rates) [35–40]. However, the amount of enhancement observed in the case of magnetoconvection is less compared to that observed in rotating RBC. In addition, the enhancement of thermal flux in magnetoconvection is not observed at larger values of Pr in RBM. This may be due to efficient generation of thermal plumes in rotating RBC at relatively higher values of Pr [39] in rotating RBC.

Thin boundary layers are also characteristics of a turbulent flow [41, 42]. The thickness of thermal boundary layer δ_{th} in turbulent RBC is known to scale with Ra as $\delta_{th} \sim Ra^{-\gamma}$. The exponent γ is found to lie between 0.2 and 0.3 [42]. We also investigated the role of magnetic field on the thickness of thermal boundary layer. To compute the thickness of the boundary layer (δ_{th}), we first spatially averaged the total temperature field $T(x, y, z, t)$ in horizontal plane for each frame of computed data points. This led to a temperature field, which is a function of the vertical coordinate z and dimensionless time t . A time average of a large number of frames (300 frames or more) yielded a temperature field $\langle T \rangle(z)$, which depends only on the vertical coordinate z . One such case for $Ra = 3.04 \times 10^6$, $Pr = 1.0$ and $Q = 300$ is shown in Fig. 8. It clearly shows a sharp drop in the temperature field in a thin layer of the fluid near both the boundaries. The temperature drop in the central part of the simulation cell is very small. We draw two straight lines: one drawn through the almost vertical part and another drawn through the part where the temperature drop is sharp (see Fig. 8). The estimated thermal boundary layer δ_{th} is the vertical distance of the point of intersection from the nearest boundary. The upper viewgraph of Fig. 9 shows the variation of the thickness of thermal boundary layer with Q for $Pr = 1.0$ and different values of Ra . The thickness δ_{th} increases with Q for a fixed value of Ra . It is expected as the increase in Q brings down the distance from criticality ϵ . The lower viewgraph shows the variation of δ_{th} with Ra for different values of Q on log-log scale. The boundary layer thickness decreases with increase in Ra for a fixed value of Q . The boundary layer thickness shows scaling behavior with Ra : $\delta_{th} \sim Ra^{-\gamma}$, where the exponent $\gamma(Q)$ now depends on the Chandrasekhar's number Q . The value of γ is found to be 0.30 ± 0.01 for $Q = 3 \times 10^2$ and 0.18 ± 0.01 for $Q = 10^3$. The value of γ is in excellent agreement with the experimental observation of Zhou and Xia [42] for lower value of Q .

We have also computed the probability distribution functions (PDFs) of the local heat fluxes in the vertical direction to investigate the role of the external magnetic field on PDFs. For this, the values of the vertical velocity v_3 and convective temperature θ are recorded at all spatial grid points at regular interval for a long time. A probability distribution function (PDF) of $v_3\theta$ is then computed for each of these frames. A time averaged PDF of local heat fluxes is then obtained using a minimum of 300 frames of computed data sets. Fig. 10 shows PDFs of the vertical local heat fluxes for $Ra = 5.0 \times 10^5$ and $Pr = 4.0$ for four different values of Q on the semi-log scale. Local heat fluxes are in the upward direction as well as in the downwards

direction. All the PDFs are asymmetric about their maxima located at $v_3\theta = 0$ and are non-Gaussian. The asymmetry of the PDF shows that the excursion of upward heat flux is more than the excursion of downward heat flux. This signifies that a net heat flux is maintained in the vertically upward direction. The data points in PDFs shown by blue (black) squares, pink (light gray) circles, magenta (gray) stars and green (gray) triangles are for $Q = 70, 50, 300$ and 500 , respectively. The time averaged PDFs of local thermal fluxes in the vertical direction show a cusp at the maximum. This type of cusp was first observed in experiment on turbulent RBC [43]. The PDF of instantaneous local fluxes in the vertical direction also showed the cusp at the maxima in simulations [44]. It may be due to non-Gaussian nature of the vertical velocity v_3 and the convective temperature θ . The inset of Fig. 10 shows an enlarged view of the PDFs near their maxima. The time averaged PDFs with wider spread have lower values of maxima. For $Ra = 5.0 \times 10^5$ and $Pr = 4.0$, the largest spread of a PDF is for $Q = 70$. The histograms for these cases have exactly the similar shapes (not shown here) and they show the time averaged vertical local heat flux is maximum for $Q = 70$, which correspond to $\sqrt{Ra/(QPr)} = 42.25$ for $Pr = 4.0$. This is consistent with the largest global heat flux for $Q = 70$ for the same set of all parameters (see Fig. 6). The probability distribution functions of the local heat fluxes show exponential tails. A large part of the distribution function for the upward local heat flux may be represented with two exponential functions, while the distribution function for the downward local heat flux can be represented well by a single exponential function. It is interesting to note that local energy flux shows approximately exponential tails in wave turbulence [45]. However, the anisotropy in a thermally stratified system makes the probability distributions of local heat fluxes in vertical direction asymmetric on two sides of the peak.

5. Conclusions

A numerical study on global as well as local heat fluxes in Rayleigh-Bénard magnetoconvection in different fluids is presented. The global heat flux of unsteady magnetoconvection with a uniform vertical magnetic field shows a mild enhancement as the strength of the uniform magnetic field is raised for relatively lower values of Q and a range of thermal Prandtl number ($0.1 \leq Pr \leq 4.0$). For relatively higher values of external magnetic field, there is suppression of heat flux in nanofluids, liquid crystals as well in geophysical liquid metals. The time averaged global heat flux (Nusselt number) decreases logarithmically with Chandrasekhar's number for all fluids responsive to a vertical magnetic field, when Rayleigh number and Prandtl numbers are kept at fixed values. For water based nanofluids is likely to show this behaviour, if the volume fraction of spherical copper nanoparticles is around 8%. A similar behaviour is likely in Earth's outer liquid core ($Pr \approx 0.1$) as well as some liquid crystals. The enhancement in heat flux makes the relative time averaged value of Nusselt number slightly more than unity for smaller values of the dimensionless parameter $\sqrt{Ra/(QPr)}$. The global thermal flux as well as the PDF of local heat flux confirm small enhancement of

thermal flux. The fluctuating part of the Nusselt number shows nearly normal distribution with asymmetric tails. The power spectral density of the Nusselt number scales with frequency f approximately as f^{-2} for higher values of f . The thickness of thermal boundary layer scales with Rayleigh number as $\delta_{th} \sim Ra^{-\gamma}$. For lower values of Q , $\gamma \approx 0.3$ and its value decreases as Chandrasekhar numbers is increased. The PDF of vertical local heat-fluxes is found to be non-Gaussian and asymmetric with cusp at its maximum and it has exponential tails.

Acknowledgments:

We thank both the anonymous Reviewers whose comments made us improve the manuscript significantly. Discussions with Dr. H.K. Pharasi was fruitful.

References

6. References

- [1] S. Kakac and A. Pramuanjareonkij, "Review of convective heat transfer enhancement with nanofluids", *Int. J. Heat Mass Transfer* **52** (2009) 3187-3196.
- [2] K. Khanafer and S. Aithal, "Laminar mixed convection flow and heat transfer characteristics in a lid driven cavity with a circular cylinder", *Int. J. Heat Mass Transfer* **66** (2013) 200209.
- [3] F. Selimefendigil and H.F. Öztup, "Numerical study of MHD mixed convection in a nanofluid filled lid driven square enclosure with a rotating cylinder", *Int. J. Heat Mass Transfer* **78** (2014) 741-754.
- [4] N. Shahcheraghi, H.A. Dwyer, A.Y. Cheer, A.I. Barakat, and T. Rutaganira, "Unsteady and Three-Dimensional Simulation of Blood Flow in the Human Aortic Arch", *Trans. ASME* **124** (2002) 378-387.
- [5] M. Waskaas and Y.I. Kharkats, "Magnetoeconvection Phenomena: A Mechanism for Influence of Magnetic Fields on Electrochemical Processes", *Phys. Chem. B* **103** (1999) 4876-4883.
- [6] R.W. Series and D.T.J. Hurler, "The use of magnetic fields in semiconductor crystal growth", *J. Crystal Growth* **113** (1991) 305-328.
- [7] P.A. Davidson, "Magnetohydrodynamics in Materials Processing", *Annu. Rev. Fluid Mech.* **31** (1999) 273-300.
- [8] P. Olson and G.A. Glatzmaier, "Magnetoeconvection and thermal coupling of Earth's core and mantle", *Phil. Trans. R. Soc. Lond. A* **354** 1413-1424.
- [9] G.A. Glatzmaier, R.S. Coe, L. Hongre, and P.H. Roberts, "The role of the Earth's mantle in controlling the frequency of geomagnetic reversals", *Nature*, **401** (1999) 885-890.
- [10] J. Marshall and F. Schott, "Openocean convection: Observations, theory, and models", *Rev. Geophys.* **37** (1999) 1-64.
- [11] F. Busse and W. Pesch, "Thermal convection in a twisted horizontal magnetic field", *Geophys. Astrophys. Fluid Dyn.* **100** (2006) 139-150.
- [12] P.H. Roberts and E.M. King, "On the genesis of the Earth's magnetism", *Rep. Prog. Phys.* **76** (2013) 096801.
- [13] R. Beck, A. Brandenburg, D. Moss, A. Shukurov, and D. Sokoloff, "GALACTIC MAGNETISM: Recent Developments and Perspectives", *Annu. Rev. Astron. Astrophys.* **34** (1996) 155-206.
- [14] F. Cattaneo, T. Emonet, and N. Weiss, "On The Interaction Between Convection and Magnetic Fields" *Astrophys. J.* **588** (2003) 1183-1198.
- [15] M.J. Thompson and J. Christensen-Dalsgaard, *Stellar Astrophysical Fluid Dynamics*, Cambridge University Press, Cambridge (2003).
- [16] D. Ryu, H. Kang, J. Cho, and S. Das, "Turbulence and Magnetic Fields in the Large-Scale Structure of the Universe", *Science* **320** (2008) 909-912.
- [17] S. Chandrasekhar, "Hydrodynamic and Hydromagnetic Stability", Oxford University Press, London (1961)
- [18] S. Fauve, C. Laroche, A. Libchaber, and B. Perrin, "Chaotic Phases and Magnetic Order in a Convective Fluid", *Phys. Rev. Lett.* **52** (1984) 1774-1777.
- [19] N.O. Weiss and M.R.E. Procter, "Magnetoeconvection", Cambridge University Press, Cambridge (2014).
- [20] A. Basak, R. Raveendran, and K. Kumar, "Rayleigh-Bénard convection with uniform vertical magnetic field", *Phys. Rev. E*, **90** (2014) 033002.
- [21] S. Cioni, S. Chaumat and J. Sommeria, "Effect of a vertical magnetic field on turbulent Rayleigh-Bénard convection", *Phys. Rev. E* **62** (2000) R4520-R4523.
- [22] J.M. Aurnou and P.L. Olson, "Experiments on Rayleigh-Bénard convection, magnetoconvection and rotating magnetoconvection in liquid gallium" *J. Fluid Mech.* **430** (2001) 283-307.
- [23] U. Burr and U. Müller, "Rayleigh-Bénard convection in liquid metal layers under the influence of a vertical magnetic field", *Phys. Fluids* **13** (2001) 3247-3257.
- [24] J. Maxwell, "A Treatise on Electricity and Magnetism", Oxford University Press, London (1873).
- [25] H. Brinkman, "The viscosity of concentrated suspensions and solutions", *J. Chem. Phys.* **20** (1952) 571581.
- [26] B. Lee, J. Z. Liu, B. Sun, C. Y. Shen, and G. C. Dai, "Thermally conductive and electrically insulating EVA composite encapsulants for solar photovoltaic (PV) cell", *Express Polym. Lett.* **2** (2008) 357-363.
- [27] R.J. Goldstein and D.J. Graham, "Stability of a Horizontal Fluid Layer with Zero Shear Boundaries", *Phys. Fluids* **12** (1969) 1133-1137.
- [28] G. Veronis, "Large amplitude Bénard convection", *J. Fluid. Mech.* **26** (1966) 49-68.
- [29] D. R. Moore and N. O. Weiss, "Two-dimensional Rayleigh-Bénard convection", *J. Fluid. Mech.* **58** (1973) 289-312.
- [30] O. Thual, "Zero-Prandtl-number convection", *J. Fluid. Mech.* **240** (1992) 229-258.
- [31] H. K. Pharasi, K. Kumar and J. K. Bhattacharjee, "Entropy and energy spectra in low-Prandtl-number convection with rotation", *Phys. Rev. E*, **89** (2014) 023009.
- [32] A. Xu, L. Shi, H-D Xi, "Lattice Boltzmann simulations of three-dimensional thermal convective flows at high Rayleigh number", *Int. J. Heat Mass Transfer*, **140** (2019) 359-370.
- [33] S. Aumaître and S. Fauve, "Statistical properties of the fluctuations of the heat transfer in turbulent convection", *Europhys. Lett.* **62** 2003 822-828.
- [34] H. K. Pharasi, K. Kumar and J. K. Bhattacharjee, "Frequency spectra of turbulent thermal convection with uniform rotation", *Phys. Rev. E*, **90** (2014) 041004(R).
- [35] Y. Liu and R.E. Ecke, "Heat Transport Scaling in Turbulent Rayleigh-Bénard Convection: Effects of Rotation and Prandtl Number" *Phys. Rev. Lett.* **79** (1997) 2257-2260.
- [36] R.J.A.M. Stevens, J.-Q. Zhong, H.J.H. Clercx, G. Ahlers, and D. Lohse, "Transitions between Turbulent States in Rotating Rayleigh-Bénard Convection", *Phys. Rev. Lett.* **103** (2009) 024503.
- [37] J.-Q. Zhong, R.J.A.M. Stevens, H.J.H. Clercx, R. Verzicco, D. Lohse, and G. Ahlers, "Prandtl-, Rayleigh-, and Rossby-Number Dependence of Heat Transport in Turbulent Rotating Rayleigh-Bénard Convection", *Phys. Rev. Lett.* **102** (2009) 044502.
- [38] S. Weiss, R.J.A.M. Stevens, J.-Q. Zhong, H.J.H. Clercx, D. Lohse, and G. Ahlers, "Finite-Size Effects Lead to Supercritical Bifurcations in Turbulent Rotating Rayleigh-Bénard Convection", *Phys. Rev. Lett.* **105** (2010) 224501.
- [39] R. J. A. M. Stevens, H. J. H. Clercx, and D. Lohse, "Optimal Prandtl number for heat transfer in rotating Rayleigh-Bénard convection", *New J. Phys.*, **12** (2010) 075005.
- [40] P. Wei, S. Weiss, and G. Ahlers, "Multiple Transitions in Rotating Turbulent Rayleigh-Bénard Convection", *Phys. Rev. Lett.* **114** (2015) 114506.
- [41] Q. Zhou and K.-Q. Xia, "Measured Instantaneous Viscous Boundary Layer in Turbulent Rayleigh-Bénard Convection", *Phys. Rev. Lett.* **104** (2010) 104301.
- [42] Q. Zhou and K.-Q. Xia, "Thermal boundary layer structure in turbulent Rayleigh-Bénard convection in a rectangular cell", *J. Fluid Mech.* **721** (2013) 199-224.
- [43] X.-D. Shang, X.-L. Qiu, P. Tong, and K.-Q. Xia, "Measured Local Heat Transport in Turbulent Rayleigh-Bénard Convection", *Phys. Rev. Lett.* **90** (2003) 074501.
- [44] O. Shishkina and C. Wagner, "Local heat fluxes in turbulent Rayleigh-Bénard convection", *Phys. Fluids* **19** (2007) 085107.
- [45] E. Falcon, S. Aumaître, C. Falcon, C. Laroche, and S. Fauve, "Fluctuations of Energy Flux in Wave Turbulence", *Phys. Rev. Lett.* **100** (2008) 064503.